

# Body Sensor Network for Mobile Health Monitoring, a Diagnosis and Anticipating System

Johan Wannenburg and Reza Malekian, *Member, IEEE*

**Abstract**—A system capable of mobile health monitoring was design and implemented from first principles. The system is capable of measuring vital physiological parameters, interpret the measured signals and provide a sense of monitoring and biofeedback to the user. In case a medical emergency is detected notifications are sent to a medical team for analysis. The system was designed through the investigation of various bio-signal extraction methods. An optical pulse oximeter sensor was designed along with the required software algorithms. The photoplethysmographic signals were extracted and used to calculate heart rate, saturation of oxygen and pulse transits time. The pulse transit time was utilized in the estimation of continuous blood pressure measurement. The pulse oximetry implementation applies reflectance based sensing on the user’s fingertip and palm. Skin temperature is also measurable through the use of a digital temperature sensor. The system is capable of providing feedback to the user by means of a smartphone application receiving data from the device via Bluetooth. The measurement of the proposed physiological parameters were successfully measured with the appropriate degree of accuracy required by medical standards. The system is capable of health monitoring by through accurate measurements, providing the user with feedback and successfully identifying medical stress resulting in the sending of a notification to a medical doctor.

**Keywords**—*Mobile health monitoring, physiological parameters, SpO<sub>2</sub>, saturation of oxygen, heart rate, photoplethysmography, PPG, blood pressure, pulse transit time, skin temperature, body sensor network, pulse oximetry, bluetooth.*

## I. INTRODUCTION

ADVANCES in modern technology have allowed for the development of miniaturized wireless mobile health monitoring systems, capable of continuous monitoring while being power efficient. Through this advancement a transformation in health monitoring is taking place, whether it be for medical or non-medical purposes, wearable body sensors are growing in popularity. A need for the development of such devices definitely exists, since they will allow for the detection of abnormalities, unforeseen situations and even provide a prognosis; all based on the monitoring of physiological parameters

This work was supported in part by the Research Development Programme, University of Pretoria.

J. Wannenburg is with the Department of Electrical, Electronic and Computer Engineering, University of Pretoria, Pretoria, 0002, South Africa. (email: johan.wannenburg@gmail.com)

R. Malekian is with the Department of Electrical, Electronic and Computer Engineering, University of Pretoria, Pretoria, 0002, South Africa. (email: reza.malekian@up.ac.za)

in conjunction with possible symptoms. Mobile health monitoring systems are capable of detecting a medical emergency and could prevent it by reporting it to medical services or by providing the user with biofeedback as an early warning; all achievable due to the implementation of continuous monitoring. The development of such systems offer flexibility and cost saving options for both healthcare professionals and patients through the implementation of continuous health monitoring. The proposed system allows for the monitoring of patients in rehabilitation, the elderly in assisted living, patients with chronic diseases and even for frequent measurements of physiological parameters on a daily basis in everyday life.

Such a system can be referred to as a Body Area Network (BAN) or a Body Sensor Network (BSN). A BAN can be defined as a network of communicating devices worn on, around or in the body, capable of providing mobile health services to the user [?]. A BAN consists of a Mobile Base Unit (MBU) responsible for the processing and communication and a set of BAN devices such as wearable sensors or actuators. In such a device, the MBU acts as the platform used for processing and as a communication gateway to a handheld device running software capable of monitoring the measured data. The processing of the data can be done on the device or remotely by a medical team [?].

This paper discusses the design and implementation of a mobile health monitoring system capable of measuring and interpreting key vitals: (1) heart rate, (2) saturation of oxygen (SpO<sub>2</sub>), (3) blood pressure and (4) skin temperature. The system was completely designed from first principles, this includes the sensor hardware, device hardware, PCB layout, software algorithms, as well as the Android application. The proposed system designed examines and implements certain functionality that solves the mentioned short comings or limitations in continuous mobile health monitoring. The device allows for flexibility, minimization of false readings and is completely capable of continuous battery powered monitoring. Background on current methods of obtaining and processing the aforementioned vital signs will be discussed, along with the design overview and implantation of the system. Obtained results that argue the validity of the device will also be discussed and concluded.

This paper is organised as follows. Section II discusses some related works that were investigated and deemed import during the development of this project. Section III provides a short description of how the system follows highlighting key functionality. In section IV, the design and implementation of the proposed system is explained; here the selected solution is justified with regards to optimisation. All findings and results are summarised in section V. Section VI sheds some light

on the possibility of future work and system improvements. Finally, the paper is concluded in section VII.

## II. RELATED WORKS

Current implementations were investigated in order to identify limitations and possible areas for improvement, specifically work done by V. Jones et al. [?] on the comparison between two types of health monitoring systems. The comparison was done in order to design a more generic open solution capable of enhanced flexibility and adaptive health monitoring in the future. The European developed device known as the MobiHealth was designed with the intent to focus on remote monitoring and treatment services while the Australian developed device, the Personal Health Monitor (PHM) was primarily focused on local (on the device) personal health monitoring. Remote monitoring allows for a reduction in device processing costs, however, delay or waiting periods for data transmission could cause other complications for real time monitoring. Local monitoring systems which allow for real time monitoring are more complex and expensive, but still provide a doctor at a remote location with biofeedback. Each of the systems have their advantages depending on the chosen desired outcome, however, it is certain that in both cases it will allow mobility of patients as well as location independent monitoring. The proposed solution would thus be a device that is suitable for measuring and processing the measured vitals locally. Once this step is completed it sends the data wirelessly to a handheld device such as a PDA or Smartphone for monitoring, as well as allowing the data to be routed to a server through either the cellular network or a Wi-Fi network.

The storage of data on a remote server will allow for trend analysis and data mining to hopefully improve medical feedback and the prediction/prevention of possible medical events [?]. The handheld device will allow the patient to observe his/her current vital signs and warn the patient when a medical emergency is taking place. Studies show that when a patient with a medical condition, in need of a lifestyle change is able to observe his/her vital signs, the device can aid and motivate a patient to achieve these lifestyle changes [?]. Patients also tend to feel more relaxed when knowing the status of their own vitals. The device should be developed with the long-term focus on allowing patients who are discharged from hospital to be monitored remotely as well as to allow the monitoring of the elderly.

The measured medical parameters and medical record of a user are meant to be kept confidential. Since information will be transferred between wireless nodes and across the internet; certain steps should be taken to ensure that sensitive information remains secure. Wireless sensor nodes connected to the internet can be built on novel ideas such as the IoT (internet of Things) to transfer data from patients to a database. The medical information stored on the database should have limited access, thus user authentication and some form of access control should be implemented to ensure that only the relevant parties have access to user medical records [?].

### A. PPG Signal Extraction

The extraction of heart rate, SpO<sub>2</sub> and blood pressure is performed by pulse oximetry through a PPG sensor. Since this sensor is responsible for obtaining 3 of the 4 specified physiological parameters it is considered the most valuable part of the sensor network and requires thorough investigation and design. Analysis of current work allowed for the realisation of the general design and breakdown of PPG sensors [?], [?], [?].

The extraction of PPG signals follows a specific set of steps, firstly, an optical sensor is used for the measurement process resulting in the output of a current. The second stage makes use of a Transimpedance amplifier allowing the measured current to be converted to a voltage to simplify processing. The signal needs to be filtered to remove any noise and DC components, once the signal has been filtered it is amplified to an acceptable range for the ADC to sample and store it. The design of this sensor is explained comprehensively in section IV since all aspects of the sensor were designed from first principles.

### B. Pulse Transit Time Detection Process

As mentioned blood pressure extraction will also make use of the pulse oximetry hardware, once the PPG signals are digitized, they are processed to detect PTT. Other implementations make use of both PPG and ECG sensors to do this, however, in this design two PPG sensors were used based on the work done by R. Teja [?]. The two PPG sensors are set up in such a way that one is leading and the other lagging. Both sensors measure PPG signals, however due to their location and relevant distances from the heart the one signal leads the other in a time domain measurement. This time is measured using designed software algorithms and used in the calculation and prediction of blood pressure. Figure 1 is used to visually describe the explained PTT acquisition process.

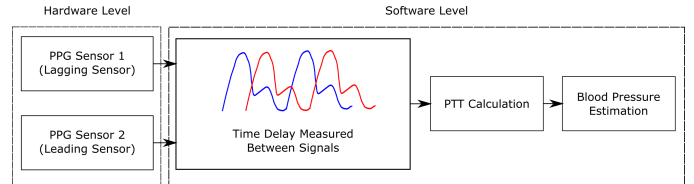


Fig. 1. Pulse transit time extraction from measured PPG signals

## III. SYSTEM OVERVIEW

A broad overview of the system shown in figure 2 explains that the system is broken down into three subsystems. These subsystems make up the core components of designed solution. Each of these subsystems perform important tasks and are integrated in a manner to optimize system performance. Subsystem 1 consists of the sensors used in the BSN, this subsystem contains the sensors that measure each of the physiological parameters specified, and this is largely focused on analog front end and the acquisition of the measured signals. The second subsystem which consist of the processing and communication unit explains the microcontroller aspect of the BSN; here focus is placed on software algorithms which extract the

required information from the measured signals and then acts accordingly to prepare information used in biofeedback to the patient. This component is also responsible for the storage of data and communication with the handheld Android smartphone, subsystem 3. The third subsystem provides the patient with biofeedback through notifications, any abnormalities found are extracted here and sent to a medical doctor to allow for monitoring of the patient. Any information sent to the medical doctor is done by the smartphone application through the utilization of the smartphone's mobile network, 3G or through a Wi-Fi network. Subsystems 1 and 2 make up the BSN implemented as a wearable battery-powered device on the patient while subsystem 3 is an Android application running on a smartphone. Bluetooth has been selected as the communications medium between the device and smartphone.

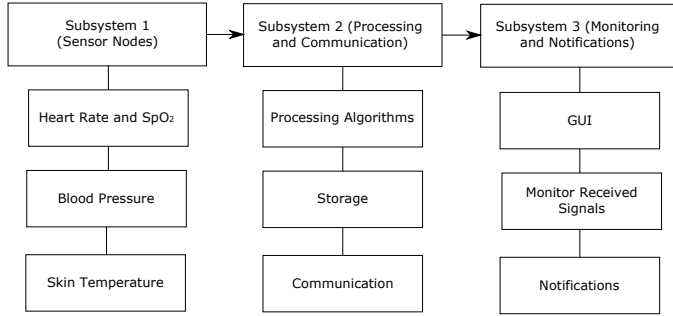


Fig. 2. Overview and breakdown of the proposed system

#### IV. SYSTEM DESIGN

##### A. Photoplethysmography

Photo based sensing on a patient's skin, more specifically areas of the skin with perforated blood flow, is used in order to obtain PPG signals. This process is based on the Beer-Lambert Law which states that the intensity of a beam of monochromatic radiation in an absorbing medium decreases exponentially with penetration distance [?]. This means that a change in the intensity of light transmitted through tissue can be measured as a voltage [?]. Analysis of arterial blood flow shows that there are two types of haemoglobin, ones that carry oxygen and others that do not. Oxygenated and non-oxygenated haemoglobin have different absorption spectra at specific wavelengths of light. Therefore, in order to measure  $SpO_2$  the haemoglobin will be bombarded with light of specific frequencies in order to maximize the absorption of the specific light by the relevant haemoglobin. The two light sources selected are as follows, one with a wavelength of 660 nm (red light) and the other with a wavelength of 940 nm (Infrared light). Oxygenated haemoglobin (HbO) absorb IR light and reflect Red light while non-oxygenated haemoglobin (Hb) absorb more Red light and reflect IR light. These wavelengths of light are specifically selected so that the percentage of oxygenated haemoglobin can be calculated by weighing it with respect to non-oxygenated haemoglobin and the total number of haemoglobin present. At 660 nm the absorption of light

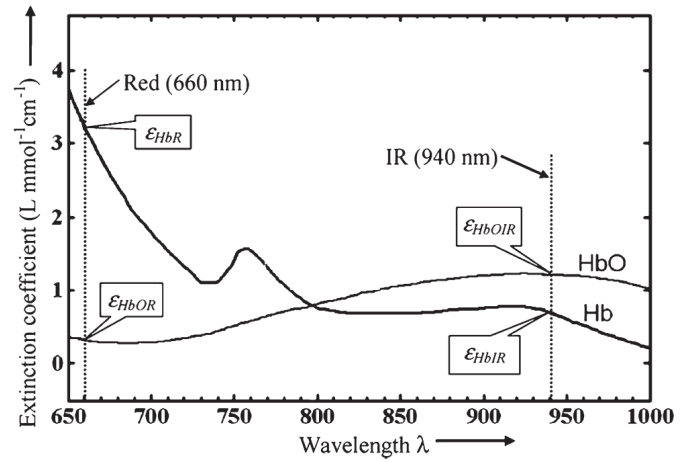


Fig. 3. Relevant light extinction coefficient vs. wavelength for the interested wavelengths of light [?].

varies greatly between the two types of haemoglobin while at 940 nm they are very similar; this allows for the use of a ratio to determine the saturation of oxygen. Figure 3 visually supports why these specific wavelengths are selected.

The ratio of the absorption at these two wavelengths of light will be used to determine the fractional part of HbO in the arterial blood, which in turn was used to calculate the saturation of oxygen [?],

$$SpO_2 = \frac{HbO}{HbO + Hb} \times 100. \quad (1)$$

(1) shows that the saturation of oxygen is simply the total percentage HbO relative to the total percentage haemoglobin. Using pulse oximetry and obtaining voltage measurements for both IR and red light the  $SpO_2$  can be calculated by taking their respective AC and DC components into account. The measured AC and DC amplitudes of the red and IR light are normalized to a parameter known as the R ratio explained by (2) [?],

$$R = \frac{AC_R/DC_R}{AC_{IR}/DC_{IR}}. \quad (2)$$

Where  $AC_R$  and  $AC_{IR}$  refer to the AC amplitudes of the signals and  $DC_R$  and  $DC_{IR}$  to the respective DC values. The DC component of the signal is affected by the absorption in the light source's intensity, ambient light influences, non-pulsatile arterial blood, venous and capillary blood, bone and muscle. The AC component consists of the pulsating arterial blood which is located on top of the DC component. The AC signal was calculated as the total span of the PPG signal using (3), while the DC signal was chosen as the minimum peak value of the AC PPG signal (4).

$$AC = Peak_{Max} - Peak_{Min} \quad (3)$$

$$DC = Peak_{Min} \quad (4)$$

Once the R ratio is known  $SpO_2$  can be determined through experimentation by setting up a calibration curve. The calculated R ratio and  $SpO_2$  are related with an empirical formula which is almost linear and derived by calibration [?]. This calibration is done through curve-fitting data acquired from volunteers, an example of such a curve is shown in figure 4. Once the data is plotted, a linear approximation can be made to determine a straight line equation of the form,

$$SpO_2 = A \cdot R + B. \quad (5)$$

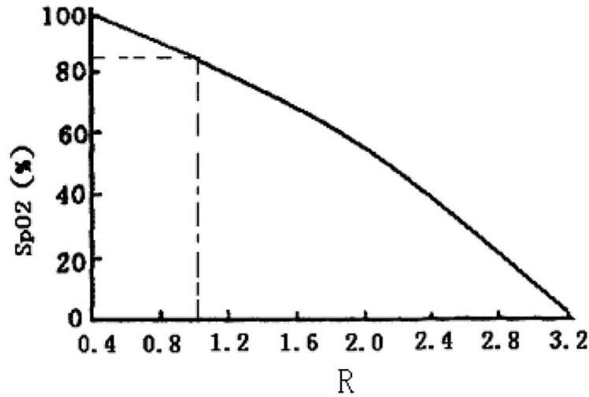


Fig. 4. Relationship between the R ratio and  $SpO_2$  [?].

Where R is the R ratio, A and B are constants in the straight line equation. The straight line equation allows the calculation of  $SpO_2$  from the measured R ratio. Since PPG follows cardiac rhythm the signal was used to determine the patient's heart rate. This was done by measuring the period between maximum peaks of the measured PPG signal and multiplying it by 60 (1 minute) to obtain a measurement per minute; this is described by the following equation,

$$BPM = Frequency \times 60. \quad (6)$$

This resulted in a rapid changing measurement since it was calculated between each successive maximum peaks, thus a smoothing factor was applied to average the heart rate calculation. The final heart rate provided was therefore an average of a total of 5 heart rate measurements, allowing the removal of possible noise in slightly inaccurate measurements.

### B. PPG Sensor

The photo sensor implemented is made up of two parts, a transmitter and a receiver. The transmitter consists of LEDs (IR and Red) which serve as the light sources at different wavelengths and the receiver a photo detector such as a Photodiode. Two types of sensing exists namely reflective and transmissive, where in reflective sensing the transmitter and receiver are situated on the same side of the tissue and in transmissive sensing the transmitter and receiver are located on opposite sides of the tissue. Reflective sensing was implemented due to the fact that transmissive sensors can only be applied to thinner or peripheral parts of the body. The other disadvantage of using

a transmissive based sensor is the fact that when there is a drop in perfusion an accurate measurement cannot be ensured [?].

As mentioned pulse oximetry was used to measure a PPG signal which will be used in order to derive both heart rate and  $SpO_2$ , this sensing nodes hardware aspect is also used to acquire the signal for measuring and calculating blood pressure, which will be explained at a later stage. Figure 5 presents a graphical explanation of how the implemented sensing node functions.

For the implementation of the receiver a photodiode was used rather than a phototransistor since it yields a much faster response. The measured (reflected) light induces a current in the photodiode which is converted to a voltage by the transimpedance amplifier. The transimpedance amplifier is designed with to be stable over a wide range of frequencies, and filters out high frequency noise. When calculating  $SpO_2$  the oxygen content of the haemoglobin needs to be determined. The photodiode will detect the reflected light, however, the light absorbed by the haemoglobin needs to be used to determine the oxygen levels. Therefore, the signal needs to be inverted to produce the absorbed light, this is implemented in the transimpedance amplifier stage.

Since the system consists of two transmitters and only one receiver, the received signals was separated into a Red and an IR component. This stage was implemented through the uses of a Single-Pole-Double-Throw SPDT analog switch. This component receives one signal but can select one of two output channels by changing the state of the channel select pin which is driven by a clock signal. The channel selection pin is controlled by the microcontroller and follows the timing pattern used to control the LED driver. The PPG signal is passed through a 50 Hz notch filter in order to suppress any noise components produced by artificial light falling onto the patient's skin or from power lines [?]. The implemented amplification stage makes use of non-inverting op-amp (operational amplifier) configurations as the signal should not be inverted again. The AC signals have an amplitude in the microvolt range, which means that a large gain should be applied in order to amplify the signal to the range of the ADC. One of the challenges faced with in this design is the fact that the device needs to be portable and battery powered. This means the op-amps need to run between 0 and 5 V, therefore a virtual ground was established at half of the supply voltage ( $V_{CC}$ ). This virtual ground was generated by a voltage divider followed by a buffer and is used as a reference in each of the op-amp circuits. Another problem faced in hardware are motion artifacts or a fluctuation in the signal, this might cause the amplified signal to saturate which is undesired. To counter this effect an automatic reference selector was implemented to remove all DC components before amplification. This can also simply be implemented through the elimination of the DC component by AC coupling capacitors.

Once the signal is amplified it is passed to an anti-aliasing low pass filter which removes any high frequency noise and ensures the signal integrity when being sampled by the microcontroller's ADC, this filtering also ensure that the desired frequency range is isolated and preserved. The frequency range of interest is between 0.1 Hz and 5 Hz. A lower cut-off was

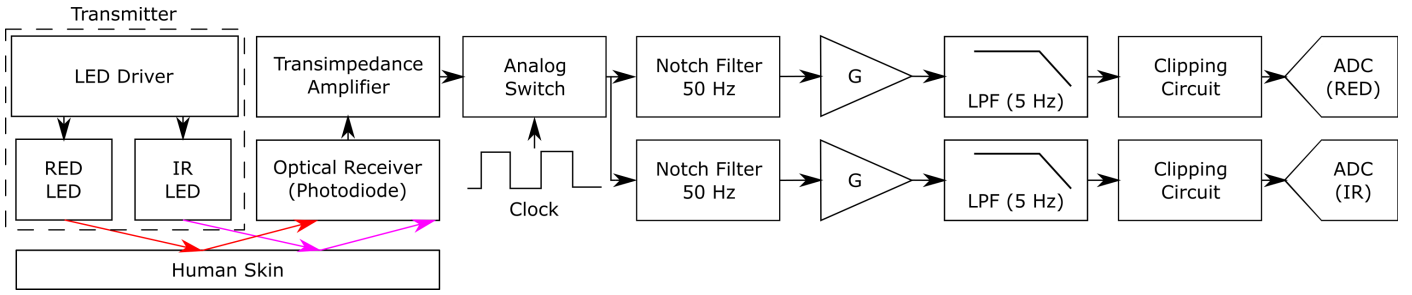


Fig. 5. System level overview of the implemented PPG sensor

implemented to eliminate the DC component and an upper cut-off was set to 5 Hz as this is the equivalent of a heart rate of 300 BPM. Active 2nd order Butterworth filters were implemented as they provide the required cut-off and are not complicated to implement when using the KRC equal component design. As mentioned the op-amps is powered by a 5 V supply while the microcontroller ADC is limited at 3.3 V, thus a protection method, the clipping circuit was implemented in order to protect the microcontroller's analog port.

### C. Hardware Design of PPG Sensor

This section highlights some of the key design aspects of the implemented PPG sensor, the core functional blocks explained in the previous section and shown in figure 5 are discussed here along with the justification of specific design selections.

#### 1) Virtual ground generation and op-amp configuration:

In the design of the hardware and sensors a single supply solution was selected as opposed to a dual supply solution, this implementation was selected in order to simplify hardware and power supply designs. The single supply configuration resulted in the use of CMOS single supply, rail-to-rail op-amp devices, which would yield the best signal outputs. This meant that only a 5 V single supply is required and that the peak-to-peak output voltage would be maximized across this voltage range. Using single supply op-amps means that when ground is selected as the reference the signal will be clipped as the AC component will exist about the reference voltage, thus the measured signal will end up being corrupted since half of the signal will be a negative voltage. To correct this a "virtual ground" needs to be generated to act as a reference, this virtual ground is designed to be half of the full scale ADC voltage range which is 3.3 V, therefore, the virtual ground is situated at 1.65 V. This was selected in order to use the entire ADC voltage range, and allows for maximum signal quality scaling.

The virtual ground is generated using a resistor voltage divider network followed by a buffer. The buffer is used to allow a high input impedance to allow for circuit protection, the virtual ground is also a net that is required throughout the analog front end as a reference, therefore the buffer will provide a stable output. The virtual ground voltage is

calculated by

$$\begin{aligned} V_{out} &= \frac{R_2}{R_1 + R_2} \times V_{cc} \\ &= \frac{10k\Omega}{10k\Omega + 10k\Omega} \times 3.3V \\ &= 1.65V \end{aligned} \quad (7)$$

where  $V_{cc}$  is the 3.3 V supply and  $V_{out}$  the virtual ground. The desired virtual ground should be half of the supply voltage, so in this case 1.65V.  $R_1$  and  $R_2$  are selected equal to obtain this voltage. The following figure shows the circuit diagram for obtaining the virtual ground output denoted as  $VIRT\_GND$ .

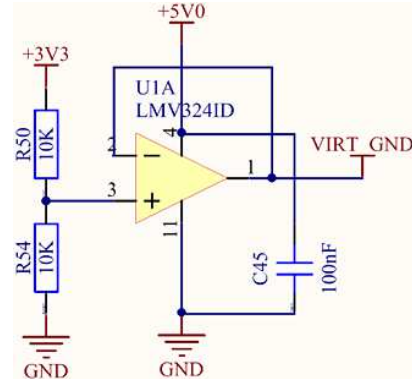


Fig. 6. Representation of virtual ground circuit configuration.

2) *Transimpedance amplifier*: The most important aspect of the PPG sensor is the optical receiver, this part of the sensor will determine the input signal quality. As explained a photodiode was used followed by a transimpedance amplifier (TIA) circuit to convert the measured current to a voltage, the TIA circuit can be seen in figure 7. The photodiode is biased in order to compensate for the required signal inversion. The virtual ground voltage is used to bias the photodiode and for the reference voltage of the TIA, this sets a reference at half of the supply voltage. The output voltage of the TIA is obtained by using the following formula:

$$V_{out} = I_S R_F \quad (8)$$

Here  $I_S$  is the current flowing through the photodiode and  $R_F$  the feedback resistor responsible for the gain.  $R_F$  should be selected to provide a high gain to the input current  $I_S$  so that the op-amp's output voltage swing is utilized optimally. The output voltage of the TIA was selected as close to the virtual ground voltage as possible, and the short circuit current of the photodiode is roughly  $20 \mu A$ . Using (8)  $R_F$  can now be calculated since the expected voltage and current is known.

$$\begin{aligned} R_F &= \frac{V_{out}}{I_S} \\ &= \frac{1.65V}{20\mu A} \\ &= 82.5k\Omega \\ &\approx 82k\Omega \end{aligned} \quad (9)$$

An  $82 k\Omega$  resistor is selected for  $R_F$  since this is a standard E12 resistor value. A TIA design also requires the analysis of stability criterion in order to avoid oscillation, capacitor  $C_F$  is used to stabilize the TIA circuit. Calculating  $C_F$  requires some other equations in order to calculate the capacitor for adequate stability. Other capacitances that exist in the circuit need to be considered such as the photodiode's output capacitance  $C_{SNS}$  and the op-amp's common and differential mode capacitances,  $C_{CM}$  and  $C_{DM}$ . These capacitances added together are referred to as  $C_S$  and is used to determine the crossover frequency ( $f_{XVR}$ ) which will be used to calculate the required capacitor value for stability compensation. The value for the compensation capacitance  $C_C$  can be calculated by means of the following equation.

$$\begin{aligned} C_C &= 2 \left( \frac{1}{2\pi f_{XVR} R_F} \right) - C_{R_F} \\ &= 2 \left( \frac{1}{2\pi \times 578.41Hz \times 82k\Omega} \right) - 0.2pF \\ &= 6.2pF \end{aligned} \quad (10)$$

Here  $C_{R_F}$ , the capacitance value of resistor  $R_F$  is assumed as  $0.2 pF$  for a 0805 SMD resistor. The capacitor  $C_F$  can be calculated from  $C_C$  by adding  $0.2 pF$  to compensate for the 0805 SMD package capacitances. Thus resulting in  $C_F = 6.4pF$ , a value of  $10 pF$  was selected as this was the closet available capacitor value that could be obtained.

Lastly noise reduction in the TIA is required, this will eliminate any high frequency noise components due to either light detected by the photodiode or internally generated op-amp noise. This will be implemented through the use of a passive low pass filter that consists of  $R_N$  and  $C_N$ . The low pass filter should have a cut-off frequency low enough to suppress high frequency components caused by the switching frequency of the modulated signals received. A cut-off frequency of around  $500 Hz$  was selected, the calculation for  $R_N$  and  $C_N$  are as

follows:

$$f_c = \frac{1}{2\pi R_N C_N} \quad (11)$$

Here  $f_c = 500 Hz$  is the cut-off frequency of the low pass filter, select  $R_N = 10k\Omega$ , solving for  $C_N$ ,

$$\begin{aligned} C_N &= \frac{1}{2\pi R_N f_c} \\ &= \frac{1}{2\pi \times 10k\Omega \times 500Hz} \\ &= 31.83nF \\ &\approx 33nF \end{aligned} \quad (12)$$

A standard value for  $C_N$  is selected as  $33 nF$ , which yields a cut-off frequency of  $482.29 Hz$  which is deemed acceptable for the filters intended design. Figure 7 depicts the final circuit implemented for the optical receiver.

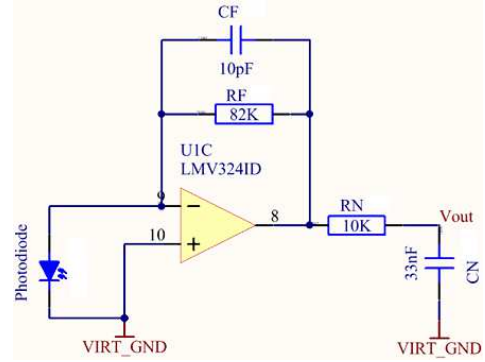


Fig. 7. Optical receiver and TIA circuit implementation.

3) *Notch filter*: The notch filter is designed to suppress  $50 Hz$  interference, these could be due to artificial light falling on the skin or due to electromagnetic interference from powerlines. A twin T passive notch filter was implemented, this topology consists of 3 resistors and 3 capacitors. A circuit diagram of the configuration is shown in figure 8. The design of the filter component values make use of the following design equations.

$$f_c = \frac{1}{2\pi R_1 C_1} \quad (13)$$

$$R_1 = R_2 = 2R_3 \quad (14)$$

$$C_1 = C_2 = \frac{1}{2} C_3 \quad (15)$$

By selecting  $f_c = 50 Hz$ , and choosing a capacitor value for  $C_1 = 100nF$ , the value for  $R_1$  can be calculated by

rearranging (13) above.

$$\begin{aligned}
 R_1 &= \frac{1}{2\pi C_1 f_c} \\
 &= \frac{1}{2\pi \times 100nF \times 50Hz} \\
 &= 31.83k\Omega \\
 &\approx 33k\Omega
 \end{aligned} \tag{16}$$

The closest E12 valued resistor available would be 33 k $\Omega$ , this will yield  $f_c = 48.23$  Hz which is very close to 50 Hz and is acceptable. The rest of the resistor and capacitor values were calculated using equations 14 and 15 and are listed in table I.

TABLE I. COMPONENT VALUES OF IMPLEMENTED TWIN T PASSIVE NOTCH FILTER.

Component	Value (Standard values)
$R_1, R_2$	33k $\Omega$
$R_3$	15k $\Omega$
$C_1, C_2$	100nF
$C_3$	220nF

To ensure that the notch filter component values are sufficient simulations were done, consisting of a frequency sweep. The simulation produced results showing that when the selected frequency is at 48.23 Hz the signal is attenuated by about 32 dB which is sufficient for the implementation of the intended notch filter. Figure 8 shows the final circuit diagram of the notch filter, the virtual ground was selected as the reference to ensure signal integrity.

4) *Gain stage:* The chosen design for the gain stage needed to take multiple factors into consideration, one of the main requirements is that the signal is not to be inverted since this will alter the signal completely. Therefore, the gain stage consists of two non-inverting op-amp gain stages. The reason two separate gain stages were implemented was due to the fact that the overall gain needs to be quite large since the initial signal is only a few hundred microvolts. Using two separate gain stages in cascade allows for a higher overall gain without possible instability, this will also allow for a more tuneable gain. Another possible concern was the influence of the amplification of any DC offsets (noise), which could

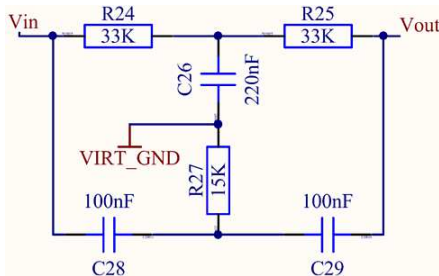


Fig. 8. 50 Hz twin T passive notch filter circuit.

result in saturation of the signal. It was decided that all DC components should be eliminated by implementing AC coupling through DC blocking capacitors at the input of each gain stage, this allows only the AC signals to pass through for amplification. Removing the DC offset means that the signal is no longer centred about the virtual ground reference, and this is corrected by biasing the input to the op-amp. In the case that any DC offset errors occur where some DC voltage is passed through or inherited from the op-amp a passive high pass filter is placed after the cascaded gain stage to eliminate DC components. Figure 9 shows the configuration of a decoupled non-inverting biased op-amp gain stage.

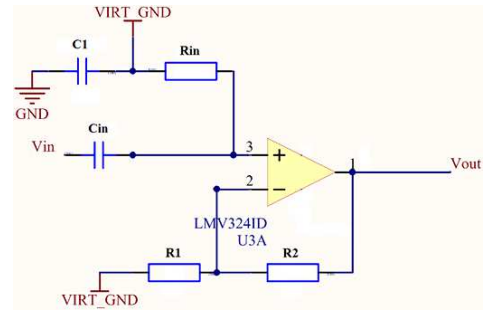


Fig. 9. The circuit diagram of the decoupled non-inverting biased op-amp gain stage.

Capacitor  $C_{in}$  is the AC coupling capacitor and was selected as 4.7  $\mu F$  which was the largest 0805 SMD capacitor available. Resistor  $R_{in}$  acts as an input impedance for AC signals and also provides a return path for the non-inverting input DC, this resistor value needs to be large in order to create a high input impedance for AC signals, and thus it is selected as 100 k $\Omega$ . The resistors  $R_1$  and  $R_2$  are used to calculate the gain of the op-amp circuit. The final capacitor  $C_1$  is included to provide stability, since this is used to bypass the voltage bias point. A rule of thumb when selecting a value for  $C_1$  is to set the pole at one-tenth the -3 dB input bandwidth which is set by  $R_{in}/C_{in}$ , the value for this capacitor was selected as 100 nF.

The system gain needs to be determined experimentally and then designed accordingly. The unamplified signal is known to be a few hundred microvolts, assuming this an estimate can be calculated based on what the amplified signal peak-to-peak voltage should be. The output voltage should be around 2 V peak-to-peak. Selecting the input peak-to-peak voltage as 1 mV the required gain is calculated by

$$\begin{aligned}
 G &= \frac{V_{out}}{V_{in}} \\
 &= \frac{2V}{1mV} \\
 &= 2000V/V
 \end{aligned} \tag{17}$$

Breaking the total gain into the two cascaded gain stages results in the following equation:

$$G = G_1 \times G_2 \tag{18}$$

Therefore the gain can be split up so that  $G_1 = 100$  V/V and  $G_2 = 20$  V/V. Calculating the gain makes use of (19) and require the selection of a resistor value and the calculation of the other. For both stages  $R_2$  will be selected as  $100$  k $\Omega$  and the following will be used to calculate  $R_1$ . The resistor values and calculations are summarised in table II.

$$V_{out} = V_{in} \left( 1 + \frac{R_2}{R_1} \right) \quad (19)$$

$$G = \left( 1 + \frac{R_2}{R_1} \right)$$

TABLE II. GAIN STAGE DESIGN SUMMARY.

	Value (Gain Stage 1)	Value (Gain Stage 2)
Gain	100V/V	20V/V
$R_1$	100k $\Omega$	100k $\Omega$
$R_2$	1.01k $\Omega$	5.26k $\Omega$
Gain with standard values	101V/V	18.86V/V
$R_1$ (Standard value)	100k $\Omega$	100k $\Omega$
$R_2$ (Standard value)	1k $\Omega$	5.6k $\Omega$

Analysing the cascaded gain based on the standard resistor values the overall gain is 1904.86 V/V which is deemed sufficient. Simulations were done to see what results should be expected based on the design of the gain stage. For the simulation an AC input signal is selected with a peak-to-peak voltage of  $700$   $\mu$ V at a frequency of  $1.5$  Hz which is considered an average frequency in the bandwidth of interest. From the simulation results the obtained output voltage was centred about the virtual ground which is  $1.65$  V and the peak-to-peak voltage is about  $2.3$  V, these are sufficient for the intended amplification application. As mentioned a passive high pass filter is implemented after the gain stage to remove any DC offsets. This filter should have a cut-off very close to DC ( $0$  V) and is thus selected as  $0.06$  Hz. Figure 10 shows the final circuit diagram of the 2 cascaded gain stages.

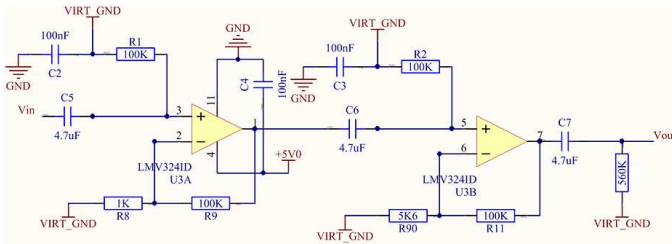


Fig. 10. Final circuit diagram of the 2 cascaded gain stages.

5) *Anti-aliasing filter*: The anti-aliasing filter implemented as an active lowpass filter was used to band limit the amplified signal. This filter also allows for the implementation of oversampling, this concept allows for a wider separation between the desired signal and most noise components. The frequency range of interest is between  $0.5$  and  $3.33$  Hz since the required BPM ranges between  $30$  and  $200$  BPM. The low pass filters

cut-off is located at  $5$  Hz to ensure the highest frequency of interest is not attenuated. The minimum stopband attenuation is an important factor to consider when designing an anti-aliasing filter. The system ADC utilized has a resolution of  $10$  bits, therefore the stopband attenuation can be calculated by

$$A_{min} = 20 \log \left( \sqrt{1.5} \times 2^B \right)$$

$$= 20 \log \left( \sqrt{1.5} \times 2^{10} \right) \quad (20)$$

$$= -61.97dB$$

Where  $B$  denotes the number of bits of the ADC. As mentioned oversampling will allow for noise shaping and move the unwanted signal components outside the filter's passband. Based on experiments and optimizations it was concluded that the signal should be sampled at  $100$  Hz. The selected sampling rate allows for an optimisation when considering the software processing algorithms since this is selected to benefit the process. Oversampling the signal at  $100$  Hz allows for a better effective resolution, this can be confirmed by the mathematical relationship in (21). If the sampling frequency  $F_s = 100$  Hz,  $f_{max} = 5$  Hz and  $B_1 = 10$  bits then  $B_2$  needs to be calculated.

$$2^{-2(B_2-B_1)} = \frac{2f_{max}}{F_s}$$

$$2^{-2(B_2-10)} = \frac{10Hz}{100Hz} \quad (21)$$

$$B_2 = 11.66 \text{ bits}$$

This means that due to oversampling the signal the  $10$  bit ADC achieves the equivalent performance of an  $11$ -bit ADC. This is done so that in-band quantization noise power is reduced. A 4th order KRC equal component lowpass filter was implemented, this means that the filter topology will make use of  $2$  stages. Equal component in KRC imposes that  $R_1 = R_2 = R$  and  $C_1 = C_2 = C$ , this solution simplifies the design. The design equations used to calculate the component values, the gain and the Q factor are as follows:

$$RC = \frac{1}{2\pi f_c} \quad (22)$$

$$K = 3 - \frac{1}{Q} \quad (23)$$

$$R_B = (K - 1) R_A \quad (24)$$

For a 4th order Butterworth low pass filter design the Q factors for each stage should be as follows:

$$Q_1 = 0.541$$

$$Q_2 = 1.306 \quad (25)$$

Using equations 22–24 the resistors and capacitor values were obtained and are listed in table III. Figure 11 shows the circuit diagram of the anti-aliasing filter implemented.

TABLE III. 4TH ORDER KRC BUTTERWORTH FILTER DESIGN SUMMARY.

	Stage 1	Stage 2
$R_1, R_2$	$68k\Omega$	$68k\Omega$
$C_1, C_2$	$470nF$	$470nF$
$R_A$	$10k\Omega$	$10k\Omega$
$R_B$	$1.5k\Omega$	$12k\Omega$
Gain	$1.15V/V$	$2.2V/V$

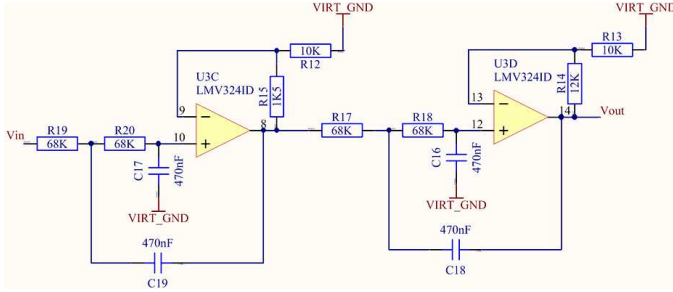


Fig. 11. Final circuit of the anti-aliasing filter, which is a 4th order low pass Butterworth filter.

6) *Clipping circuit*: As mentioned, the microcontroller's ADC can only measure in voltage range from ground ( $GND$ ) to  $V_{DD} \pm 0.3 V$ , where  $V_{DD}$  is the 3.3 V supply of the microcontroller. The output signal of the anti-aliasing filter is driven by the op-amp, therefore it could possibly have a maximum voltage of 5 V, if the signal saturates it could cause damage to the ADC, thus a circuit needs to be implemented to protect the ADC. This was implemented using a clipping circuit which consists of two diodes used to clamp the voltage at ground and 3.3 V. Since there is a voltage drop across a diode, this also needs to be taken into consideration in the design. If the diode clamping the voltage to the upper limit is connected to  $V_{DD}$ , then the circuit will clamp the voltage at 3.3 V plus the voltage drop across the diode ( $V_D$ ), which is typically 0.7 V, this will not protect the ADC. The proposed solution was to generate a reference voltage to compensate for the voltage drop across the diode. The diodes used have a slightly higher voltage drop than 0.7 V, approximately 0.85 V. The following shows this relationship mathematically.

$$\begin{aligned} V_{clamp+} &= V_{clip} + V_D \\ &= 2.35V + 0.85V \\ &= 3.2V \end{aligned} \quad (26)$$

Figure 12 shows the implemented clipping circuit, it also includes a capacitor connected in parallel to the ADC input. This capacitor serves as an external loading capacitor as well as a final noise filter for high frequencies.

#### D. Blood Pressure Estimation Through Pulse Transit Time

For blood pressure estimation, pulse transit time calculation was used. The mathematical relationship between PTT and

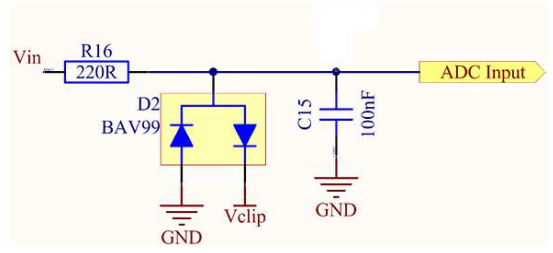


Fig. 12. The clipping circuit implemented to protect the ADC.

TABLE IV. EQUATION 27 VARIABLE DEFINITIONS [?]

Variable	Definition
$F$	Force exerted on blood
$d$	Distance from heart to fingertip
$m$	Mass of blood
$v$	Pulse wave velocity
$g$	$9.81 m/s^2$
$h$	Height difference between the two sites

blood pressure was implemented according to work done by P. Fung et al. [?], as well as certain assumptions. Laminar blood flow from the heart chamber to the fingertip through a rigid pipe (the artery) is assumed. The assumption of artery walls contracting and expanding leads to the assumption of a small compliance of 0.0018 liter/mmHg on average. This model estimates the pressure difference between two locations, in this case between the heart, from where the blood is pumped, to the finger tip, the location of the sensor. This is done through the use of Pulse Wave Velocity (PWV) which uses the distance between the two locations and the time, PTT. The work done by a pulse wave can be expressed in terms of the kinetic energy of the wave and its gravitational potential energy [?]:

$$F \times d = \frac{1}{2}mv^2 + mgh \quad (27)$$

Where each variable in (27) is described in table IV. Force can be defined in terms of pressure difference:

$$F = \Delta BP \cdot a, \quad (28)$$

Here  $a$  is defined as the cross-sectional area of the artery. When substituting equations 28 into 27 and after some rearrangement, the following equation is found,

$$\Delta BP = \frac{1}{2} \frac{m}{a \cdot d} + \frac{m}{a \cdot d} gh \quad (29)$$

In this equation  $\frac{m}{a \cdot d} = \rho$ , the density of blood and  $v$  the pulse wave velocity can be redefined as  $\frac{d}{PTT}$  [?], which is just a representation of the velocity formula  $v = \frac{x}{t}$ ,  $x$  denoting the distance and  $t$  the time. Once these new representations have been substituted into (29), the equation in (30) is obtained.

$$\Delta BP = \frac{1}{2} \rho \frac{d^2}{PTT^2} + \rho gh \quad (30)$$

Further defining some of the equation variables, the distance  $d$  can be approximated by the person's height and the average blood density  $\bar{\rho}$  is  $1035 \text{ kg/m}^3$  [?]. According to J. Keener et al. a pressure drop in the arterial side of circulation accounts for 70% of the total pressure drop in the human body. Therefore the overall blood pressure is approximately [?]:

$$\begin{aligned} BP &= \frac{\Delta BP}{0.7} \\ &= \frac{1}{0.7} \left( \frac{1}{2} \rho \frac{d^2}{PTT^2} + \rho gh \right) \\ &= \frac{A}{PTT^2} + B \end{aligned} \quad (31)$$

In conclusion the blood pressure can be written in terms of PTT and two variables  $A$  and  $B$ , where  $A$  is an estimation of the person's height [?].

$$A = (0.6 \times \text{height})^2 \times \frac{\rho}{1.4} \quad (32)$$

To determine  $B$  is not as simple, this requires recursive calibration between the estimated blood pressure and blood pressure measured by a cuff or any calibrated form of BP measurement. Calibration adapts only  $B$  since  $A$  will remain fairly constant from person to person. Calculating BP in this manner describes mean BP, where laminar and non-pulsatile flow is assumed. When using a cuff the measurement is that of diastolic blood pressure and thus an estimation of the mean blood pressure [?].

As described in section III, two PPG sensors were implemented to measure PTT, a leading and a lagging PPG sensor. The primary PPG sensor measuring IR and Red light is located on the fingertip and acts as the lagging sensor, this is due to the fact that it is located further from the heart. The primary sensor is used to measure heart rate and  $\text{SpO}_2$ . The secondary (leading) PPG sensor performs measurements on the palm, this sensor only measures IR signals since there is no need to measure Red PPG signals again in order to determine PTT, only a time delayed measurement.

### E. PPG Signal Modelling

To ensure optimal design of detection algorithms a PPG test signal needed to be generated, this signal was used in setting up a test-bench for testing each designed algorithm. These algorithms provide functionality such as peak detection, frequency detection, false peak suppression, signal clipping detection and PTT estimation. The PPG signal model derived is fairly basic and is only a close estimation of what is expected from an actual measured signal. The PPG signal can be estimated as a combination of two sinusoidal signals, thus the first step is to generate equations representing each of these signals and then adding them together. The primary component of the PPG signal can be represented by,

$$PPG_{primary} = A \times \sin(2\pi f_1 t) \quad (33)$$

Here  $A$  represents the amplitude of the signal and  $f_1$  the primary frequency of the signal. The secondary component of the PPG signal is represented by

$$PPG_{secondary} = B \times \sin(2\pi f_2 t - \phi) \quad (34)$$

The amplitude of the secondary component is represented by  $B$  and is selected to be approximately half of the primary component's amplitude  $A$ . The frequency  $f_2$  is the base frequency of the secondary component and is approximately twice that of  $f_1$  in (33). The parameter  $\phi$  introduced in (34) is used to implement a phase shift between the two signal components, this was approximated as  $270^\circ$  in order to resemble measured signals. The base PPG signal is thus obtain by the following equation.

$$\begin{aligned} PPG_{base} &= PPG_{primary} + PPG_{secondary} \\ &= A \sin(2\pi f_1 t) + B \sin(4\pi f_1 t - 270^\circ) \end{aligned} \quad (35)$$

After some manipulation the relationship in (35) could also be expressed as

$$PPG_{base} = A \cos(2\pi f_1 t) - B \sin(4\pi f_1 t) \quad (36)$$

Figure 13 shows a plot of the mathematical representation of the PPG signal at a frequency of  $1.5 \text{ Hz}$ , which is typically  $90 \text{ BPM}$ . The signal's magnitude was normalised to digital values ranging from 0 to 1023, representing that of a 10-bit ADC. The x-axis represents samples stored at a sampling rate of  $100 \text{ Hz}$ .

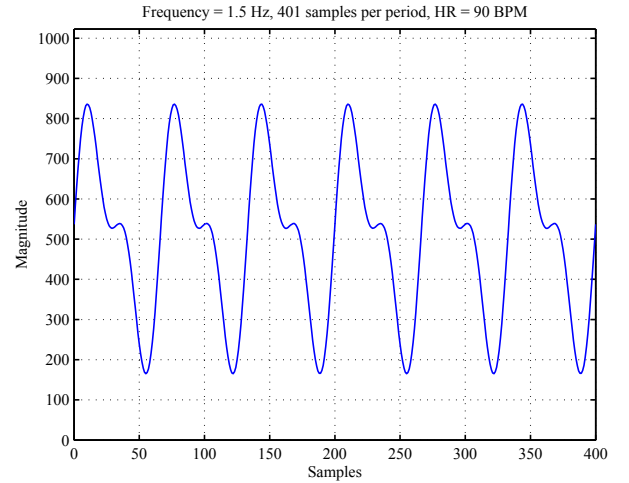


Fig. 13. Mathematical model of a pure PPG signal.

The model allows for the adjustment of various parameters such as signal amplitudes, frequency, sampling rate, phase shift, addition of signal noise, addition of signal drift, as well as addition of a DC offset. The addition of any artificial noise such as signal noise, DC offset or drift can be added to the model in order to generate a signal as close as possible to that measured in a real world scenario. The addition of signal

drift is introduced by the addition of a much slower signal where the frequency is generated at random in a given range. The introduction of a DC offset is implemented by moving the signal origin to a specified value on the x-axis. (37) shows the equation with the added noise features.

$$PPG_{final} = PPG_{base} + PPG_{drift} + PPG_{offset} \quad (37)$$

Signal noise is added to each sampled point as a random value deviating from the ideal value with a specific range, the final signal representation can be seen in the following equation. Figure 14 shows a plot of the modelled signal including noise and drift.

$$PPG_{noise} = PPG_{final} + A_{noise}PPG_{final} \quad (38)$$

where  $A_{noise}$  is the amplitude of the noise added to the signal, this amplitude is randomly generated.

This representation closely resembles that of a measured signal, and allowed for optimal design and testing of the implemented algorithms.

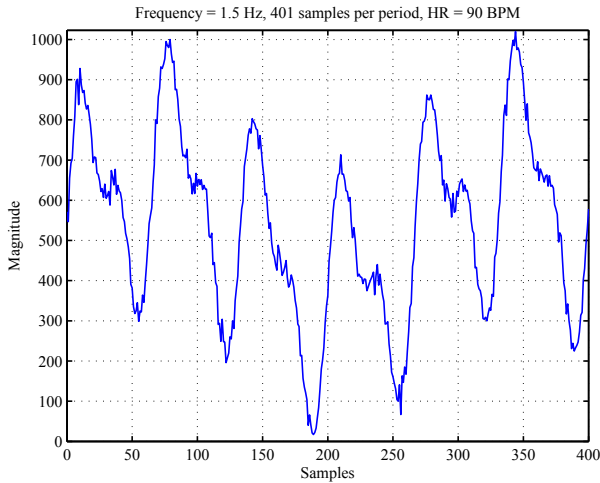


Fig. 14. Mathematical model of a noisy PPG signal.

#### F. Skin Temperature Sensor

For the measurement of skin temperature the DS18B20, a digital temperature sensor was used. This device communicates with the microcontroller via the 1-wire protocol [?]. It has a 12-bit resolution which is beneficial in detecting small temperature changes. The sensor was placed near the other sensing nodes on the patient's hand (on the palm) in order to keep all the sensors in a general area and minimize multiple leads to different locations of the body. The digital temperature sensor allowed for a linear solution which eliminates the requirements for complex calibration and design with analog sensors. This solution sacrifices hardware and calibration for a more complex software solution. The skin temperature is sampled every 30 seconds since skin temperature changes are especially slow (less than 1 Hz), approximately  $0.4 \text{ }^\circ\text{C}/\text{min}$  [?].

#### G. Device and Android Application

The final design was implemented on a double layer PCB and put into a wearable enclosure strapped onto the patient's arm. The device is battery powered and makes use of a 9 V battery stored in the device enclosure. The device microcontroller was implemented using a PIC32MX250F128D with more than enough capability in hardware and software to perform the required tasks. As for the wireless communication the RN-42N from Roving Networks was used. This device is completely programmable and configurable for parameters such as baud rate, mode of operation and many others; it also requires a small amount of external components making the design and layout less complex. Each of the connected sensors were also implemented on PCBs to allow for an optimized size since they were placed on the patient's hand. Figure 15 and 16 shows what the final device visually looks like.

The self-developed Android application was implemented on a Samsung S4 and capable of receiving and transmitting messages to/from the wearable device. The application allows for Bluetooth pairing with the device on start-up and is only functional once this pairing is deemed successful. This application is responsible for the reception of the vital parameters over Bluetooth, the processing thereof, identifying outliers caused by noise or interference, monitoring and finally notifications. Figure 17 show what the Android application looks like visually and to display what has been explained.

### V. RESULTS

#### A. Heart Rate

To verify heart rate accuracy and measurable range the device was compared with an off-the-shelf pulse oximeter. Both the device and off-the-shelf pulse oximeter were connected to 4 test subjects where both measured and logged data for one minute. Table V summarises the statistical analysis of the measured data. These results shows that the device can successfully measure heart rate with an accuracy of  $\pm 7 \text{ BPM}$  for the 203 samples taken. A 90% confidence interval was used to exclude any outliers and false measurements.

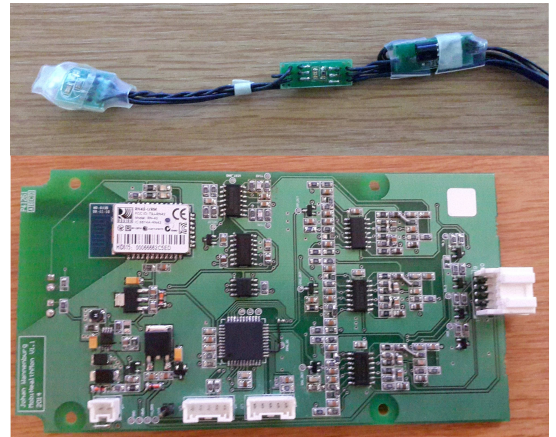


Fig. 15. Device and Sensor PCBs

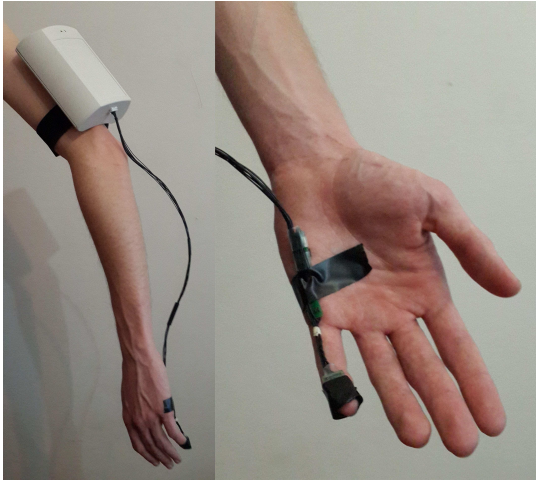


Fig. 16. Wearable device and sensors

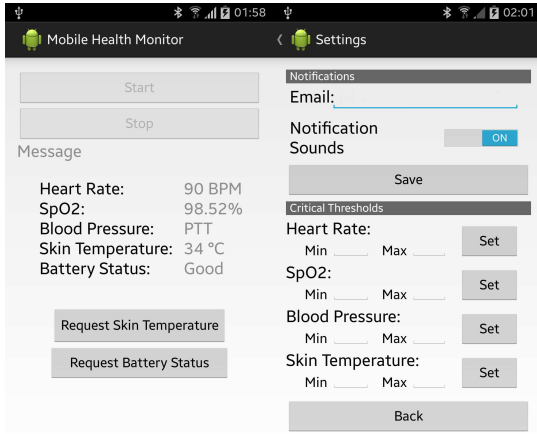


Fig. 17. Android application

The heart rate calculation algorithm was tested and verified for the required frequency range to ensure that specifications are met. In this experiment the input signal to the system ADC channels are replaced with signals generated by a function generator, this is to allow for a controlled environment where the algorithms can be tested and verified since the input is controlled. The input signal was a sinusoidal waveform with a peak-to-peak voltage of 1 V. The signals frequency was varied starting at 0.5 Hz and incremented by 0.1 Hz this was continued until 3.3 Hz. For each frequency 5 samples were taken once the signal was detected and deemed valid, these 5 samples were averaged and the result was rounded off to the nearest BPM. The results are summarised in table VI. The heart rate detection algorithm demonstrates the capability to measure heart rate between 48 to 214 BPM.

### B. Saturation of Oxygen ( $SpO_2$ )

As described in section IV the calibration curve for  $SpO_2$  measurement was derived experimentally. The R ratio measured by the device was compared to  $SpO_2$  readings from an

TABLE V. STATISTICAL ANALYSIS OF HEART RATE ACCURACY

Parameter	Value
Confidence interval	90%
Number of samples	203
Sum of squared errors	10727
Mean square error	52.842
Mean error	7.269

TABLE VI. HEART RATE DETECTION ALGORITHM RESULTS

	Minimum Frequency	Maximum Frequency	Minimum BPM	Maximum BPM
Specified	0.5 Hz	3.33 Hz	30	200
Measurable	0.8 Hz	3.57 Hz	48	214

off-the-shelf pulse oximeter. Both devices were connected to a test subject for 1 minute where R ratio and  $SpO_2$  reading were recorded and stored. The experiment was repeated on 4 different test subjects resulting in 105 samples. The collected data was used to derive a linear equation representing the relationship between R ratio and  $SpO_2$ , (39) shows the obtained linear equation.

$$SpO_2 = -1.1R + 98 \quad (39)$$

Based on the calibration curve the accuracy of  $SpO_2$  measurement was determined, this is summarised in table VII. The mean error when measuring  $SpO_2$  is 1.108 which means the % $SpO_2$  can be measured with an accuracy of 1.1%.

TABLE VII.  $SpO_2$  ACCURACY TEST RESULTS

Parameter	Value
Confidence interval	100%
Number of samples	105
Sum of squared errors	128.9525
Mean square error	1.228119
Mean error	1.108205

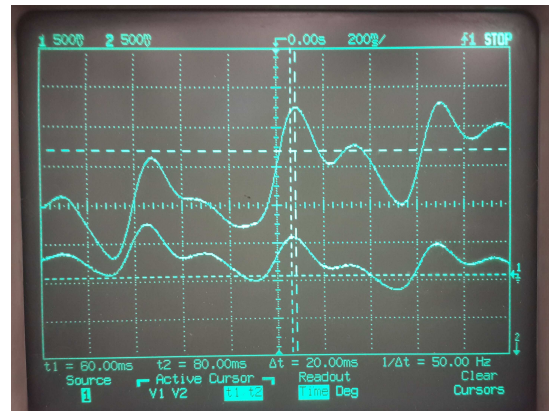


Fig. 18. PTT measurement shown on an oscilloscope.

### C. Blood Pressure

The estimation of PTT through the use of the finger and palm based PPG sensors was implemented and proved promising. The software algorithm measuring the PTT easily measured time delays of between 18-60 ms. The measured results can be seen in figure 18, this figure shows the leading and lagging sensor measurements. A time delay of 20 ms is measured between the 2 signals, it is also clear that there is a difference in the signal amplitudes measured, this is as a result of the measurement location. The larger signal is measured on the finger (lagging) where blood flow is well perfused and the small signal is measured on the palm (leading). An enhancement of the plot is visible in figure 19, this shows a simulation of the measured PTT samples, here a PTT of 20 ms is indicated. The blood pressure calibration proved somewhat complex and was thus unsuccessful, therefore, no actual blood pressure measurements were obtained. However, the proposed method of acquiring PTT with the intention of blood pressure estimation was possible and measured fairly accurate.

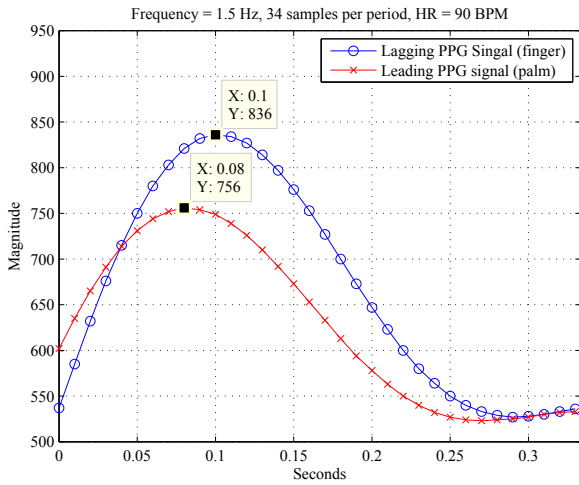


Fig. 19. Enhanced plot showing the measured PTT.

### D. Skin Temperature

To measure the accuracy of the DS18B20 digital temperature sensor it was compared to a Toptronic T802C temperature sensor. The Toptronic T802C sensor plugs into a multi-meter and gives an output of  $1\text{ mV}/^{\circ}\text{C}$ . A stopwatch was used to perform readings at set times. A pitcher containing warm water was used, this water served as the medium the experiment was conducted on. A temperature reading is taken every two minutes and recorded in a table which was used to generate a plot of the two sensors which can be seen in figure 20. The T802C makes use of a type K thermocouple which has been calibrated and has an accuracy of  $\pm 0.1\text{ }^{\circ}\text{C}$  and a resolution of  $0.1\text{ }^{\circ}\text{C}$ , while the DS18B20 is a digital temperature with an accuracy of  $0.01\text{ }^{\circ}\text{C}$ . Based on what is observed in the graph both temperature sensors follow the exact same trend, this trend is a decreasing one since the water is cooling down

over time. Even though both sensors follow the same trend the DS18B20 is always approximately  $0.25\text{ }^{\circ}\text{C}$  higher than the T802C concluding that it is accurate to  $0.25\text{ }^{\circ}\text{C}$ .

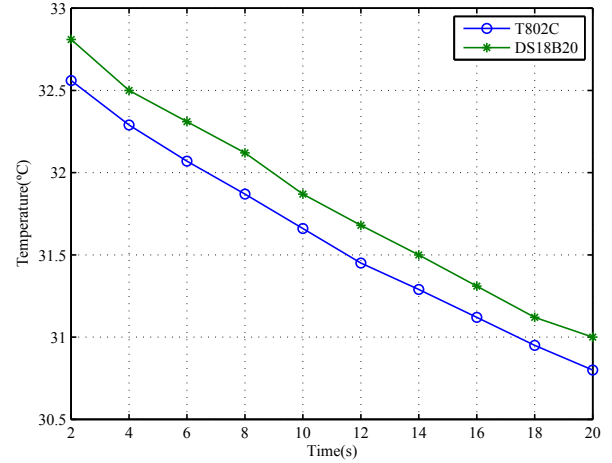


Fig. 20. Temperature sensor accuracy test results

## VI. FUTURE WORK

With respect to future work, there are some aspects that can be improved on. The main aspect to improve on would be the successful implementation of blood pressure estimation, this task requires further investigation into the calibration process. Measuring actual blood pressure requires a lengthy calibration process as some parameters are made based on assumptions, these parameters are unique to the patient and have a large influence on the measurement. Further investigation could possibly show that another method may be better suited.

The amplitude of the measured PPG signal has many external influences that can influence its size such as skin perfusion, skin temperature, measurement location, skin density, skin pigmentation and actual influences due to blood pressure changes, the prediction of such a condition is impossible. The implementation of automatic gain control would help amplify signals to the appropriate voltage levels under most conditions. The design chosen in this implementation explored the option to simplify this model and attempted to adjust the output signal by digitally controlling the PWM signals pulse widths to control LED intensity in this manner. This solution could allow for efficient power operations of the LED driver since such a system is capable of self-calibration.

## VII. CONCLUSION

The overall results achieved are very closely related to what was required and expected from the design, this means that the final implementation of the system works as intended. The solution does not only focus on the specifications but also aspects to ensure that the design is practical and that

the ultimate goal is to be able to deliver a working product. Minor improvements to the system could be made as discussed in order to improve this solution so that it is capable of measuring the required vital signs independent of most external influences. Nonetheless if the PPG signal measured on the individual is measurable, the system does achieve what it was designed to do. The overall hardware design is definitely a strong point of the system and was implemented well.

There are many aspects to improve on since the current optimal solution can always be improved. A better study and investigation on continuous blood pressure measurement using PTT is definitely something to focus on if this is to be successfully implemented, since it was found that the measurement of PTT was successful. As for the device, a PPG sensing solution that is capable of automatically calibrating and adjusting the PPG signal size in software needs to be investigated to obtain a measurable signal in almost all cases. Another development that could add value to the implemented solution would be to store all the data measured in a database for analysis and to serve as a record of a patient's vital signs. This would add value in the sense that it could make a contribution to better the understanding of the measured vitals and their relationship with specific medical conditions.

#### REFERENCES

- [1] V. Chan, P. Ray, and N. Parameswaran, "Mobile e-Health monitoring: an agent-based approach," *IET Communications*, vol. 2, no. 2, p. 223, 2008.
- [2] V. Jones, V. Gay, and P. Leijdekkers, "Body Sensor Networks for Mobile Health Monitoring: Experience in Europe and Australia," in *2010 Fourth International Conference on Digital Society*. IEEE, Feb. 2010, pp. 204–209.
- [3] B. Lo, "Architecture for body sensor networks," in *Perspectives in Pervasive Computing*. IET, Jan. 2005, pp. 23–28.
- [4] N. Ye, Y. Zhu, R. Wang, and R. Malekian, "An Efficient Authentication and Access Control Scheme for Perception Layer of Internet of Things," *Applied Mathematics & Information Sciences*, vol. 8, no. 4, pp. 1617–1624, Jul. 2014.
- [5] B. R. Teja, "Calculation of Blood Pulse Transit Time from PPG," Ph.D. dissertation, National Institute of Technology, Rourkela, 2012.
- [6] G. Ates and K. Polat, "Measuring of oxygen saturation using pulse oximeter based on fuzzy logic," in *2012 IEEE International Symposium on Medical Measurements and Applications Proceedings*. Budapest: IEEE, May 2012, pp. 1–6.
- [7] Renesas Electronics, "R178/g13 - pulse oximeter reference design," Renesas Electronics, Application Note 1, November 2011.
- [8] M. Tian, W. Liu, Z. Zhong, and Y. Pan, "Design and research on the hardware of wireless oxygen saturation detection based on ARM," in *2010 International Conference on Intelligent Control and Information Processing*. IEEE, Aug. 2010, pp. 707–710.
- [9] S. Bagha and L. Shaw, "A real time analysis of ppg signal for measurement of spo2 and pulse rate," *International Journal of Computer Applications*, vol. 36, no. 11, pp. 0975–8887, December 2011.
- [10] K. Reddy, B. George, N. Mohan, and V. Kumar, "A Novel Calibration-Free Method of Measurement of Oxygen Saturation in Arterial Blood," *IEEE Transactions on Instrumentation and Measurement*, vol. 58, no. 5, pp. 1699–1705, May 2009.
- [11] B. Venema, N. Blanic, V. Blazek, H. Gehring, A. Opp, and S. Leonhardt, "Advances in reflective oxygen saturation monitoring with a novel in-ear sensor system: results of a human hypoxia study," *IEEE transactions on bio-medical engineering*, vol. 59, no. 7, pp. 2003–10, Jul. 2012.

- [12] M. Elgendi, "On the analysis of fingertip photoplethysmogram signals," *Current cardiology reviews*, vol. 8, no. 1, pp. 14–25, Mar. 2012.
- [13] P. Fung, G. Dumont, C. Ries, C. Mott, and M. Ansermino, "Continuous Noninvasive Blood Pressure Measurement by Pulse Transit Time," in *Annual International Conference of the IEEE Engineering in Medicine and Biology Society. IEEE Engineering in Medicine and Biology Society. Annual Conference*, vol. 1. San Francisco, CA: IEEE, Sep. 2004, pp. 738–41.
- [14] R. Downs, "Using 1-Wire I/O for distributed system monitoring," in *Wescon/98. Conference Proceedings (Cat. No.98CH36265)*. Anaheim, CA: IEEE, 1998, pp. 161–168.
- [15] S. Y. Park, F. S. Nahm, Y. C. Kim, S. C. Lee, S. E. Sim, and S. J. Lee, "The cut-off rate of skin temperature change to confirm successful lumbar sympathetic block," *The Journal of international medical research*, vol. 38, no. 1, pp. 266–75, Jan. 2010.



**Johan Wannenburg** is currently pursuing the M.Eng. degree in Electronic Engineering. He received the B.Eng. degree in Electronic Engineering from the University of Pretoria, Pretoria, South Africa in 2014. He is an assistant lecturer with the Department of Electrical, Electronic and Computer Engineering at the University of Pretoria. His research interests include e-health, biosensors, body area networks, and finding novel ways of improving health monitoring through concepts such as context awareness.



**Dr Reza Malekian** (PhD, PostDoc, CEng) is a Senior Lecturer in the Department of Electrical, Electronic and Computer Engineering at the University of Pretoria, South Africa. He is also a professional member of the British Computer Society and a member of the management committee of Cost Action 1304 (ACROSS). His research lies in the area of advanced sensor networks, Internet of Things and mobile communications.